www.czasopisma.pan.pl www.journals.pan.pl

Chemical and Process Engineering: New Frontiers, 2025, 46(4), e113
DOI: 10.24425/cpe.2025.155551

Temperature field in a finite cylindrical channel with biomass transferred due to the rotation of a heated helix

Olexa Piddubniak[1], Stanisław Ledakowicz[2]*

[1] National Academy of Sciences of Ukraine, Pidstryhach Institute for Applied Problems of Mechanics and Mathematics, Naukova str., 3-b, 79060 Lviv, Ukraine
[2] Lodz University of Technology, Faculty of Process and Environmental Engineering, Wólczanska str., 215, 90-924 Lodz, Poland

Abstract
The temperature distribution field in a cylindrical channel of finite length, which was filled with moving biomass due to the rotation of an induction-heated helix, was analyzed. The outer and inner surfaces of the channel were assumed to be thermally insulated and to meet third-kind boundary conditions on temperature at the entrance and exit of the reactor. To solve the thermal conductivity problem, the desired function was decomposed into a Fourier–Bessel series with respect to the angular and radial variables. Then, an integral Laplace transformation was applied with respect to time. The exact solution was replaced by an approximate solution for practical numerical reasons. A detailed numerical analysis of the temperature field was performed. The analysis showed that the duration of the transition process was inversely proportional to the square of the biomass movement velocity and that temperature oscillation amplitudes in the quasi-stationary regime were weak. However, these oscillations are clearly manifested under space-time resonance conditions, especially when the velocities of helix rotation and rectilinear movement of the biomass are correspondingly selected. It was also determined that a local temperature increase occurs at low velocities of mass movement.

*** Corresponding author, e-mail:**
stanleda@p.lodz.pl

Article info:
Received: 26 September 2025
Revised: 13 October 2025
Accepted: 24 October 2025

Keywords
auger reactor, Joule–Lenz thermoelectric effect, temperature field, mathematical modeling, numerical analysis

1. INTRODUCTION

Recently, considerable progress has been made in improving the technological processes of pyrolysis for processing various types of waste and biomass. The results of research in this field of science and technology have been widely covered in numerous analytical reviews of global literature, primarily published between 2010 and 2020 (Biney and Gusiatin, 2024; Bridgwater and Bridge, 1991; Campuzano et al., 2019; Garcia-Nunez et al., 2017; Igliński et al., 2023; Lewandowski et al., 2019; Ore and Adebiyi, 2021; Piersa et al., 2022; Vikram et al., 2021; Winchell et al., 2022; Wu et al., 2019; Zerin et al. 2023). These reviews highlight the significant role of screw reactors in pyrolysis technologies and present the history of their creation and use for the thermal transformation of biomaterials in articles (Brown and Brown, 2012; Garcia-Nunez et al., 2017). Papers (Brassard et al., 2017; Raza et al., 2021) describe the use of screw pyrolysis reactors to create biochar and biooil. Publications (Greco et al., 2019; Perera et al., 2021) demonstrate that optimising the pyrolysis process for specific biomass materials to produce biochar with the desired properties for a given application is one of the main challenges today. At the same time, the formation of a temperature field in the reactor is identified as crucial for creating the conditions for the pyrolysis reaction.

In this regard, modeling and simulating the distribution of temperature and the movement of biomass in the reactor is of primary importance. In works (Ding et al, 2020; Jalalifar et al,. 2020; Luz et al., 2017; Luz et al. 2018; Morgano, 2019; Nachenius et al., 2015a; Rego, 2021; Sanchís et al., 2022; Shi et al. 2019), the temperature field in the reactor was simulated using computational hydrodynamics, the discrete element method and commercial mathematical support. Additionally, temperature measurements were taken experimentally. The temperature profiles were studied in particular, and it was shown that the temperature increased along the axis of the reactor from the entrance to the exit, i.e. in the direction of the general movement of biomass. The vast majority of auger reactors are heated using electric heat sources located on the lateral side of the reactor (Chojnacki et al. 2024; Fryda and Visser, 2015; Ganesapillai et al., 2023; Hasan et al., 2024; Lewandowski et al., 2019; Makkawi et al., 2022; Maximino, 2013; Obrycki et al., 2017; Proãno, 2024; Verclyte, 2013). However, pyrolysis systems have recently been developed in which the heat source is a heated screw due to the Joule–Lenz thermoelectric effect (Ledakowicz et al., 2019; Lepez and Sajet, 2009; Moser et al., 2023; Obrycki et al., 2017; Partridge et al., 2023; Pilát and Patsch, 2022; Spirajoule®, 2025). Clearly, the type of pyrolysis screw plays an important role. It should be noted that the work (Brown, 2009) drew attention to the lack of sufficient information regarding the effect of screw surface geometry on pyrolysis efficiency. Since biomass and waste are typically abrasive, sticky and poorly flowing, a standard screw shape is generally used to prevent clogging during pyrolysis.

Recently, to reduce the weight of the reactor, shaftless screws have been used (Ubiera Ruiz, 2021; Wang et al., 2015), which have screws in the form of two layers of spiral tubes filled with hot flue gas (Zhao et al., 2020; 2024). In the latter case, the effect of rotation velocity, screw pitch and spiral tube cross-section shape on pyrolysis characteristics, reactor aggregate flow and heat and mass transfer was investigated. The work (Proãno, 2024) and the patent (Obrycki et al., 2017) consider cases in which the screw is a narrow helix and the reactor contains an inner shaft. When modeling, it is important to calculate the unsteady temperature field in three dimensions (3D) in the reactor, especially when the heat source is a helix that is inductively heated by the Joule effect. Such systems have engineering applications, as discussed above. In article (Ledakowicz and Piddubniak, 2022), the authors proposed a model of the temperature field in a finite-length reactor containing a wide, electrically heated screw with a shaft. Below, we present the solution to the problem of a narrow helix screw that is heated by the Joule–Lenz effect and contains an inner shaft. As in the previous problem, a mathematical solution must be found for the heat conduction equation. This solution must take into account the velocity of biomass movement and be based on an algorithm for the numerical analysis of the spatio-temporal temperature distribution in the system depending on its parameters.

2. STATEMENT OF THE PROBLEM

Let us consider a circular ($R_1 > R_2$), length L, in which biomass (pseudo-liquefied mixture) with density ρ, heat capacity c_p and thermal conductivity coefficient λ moves in the axial direction Oz with a constant velocity v_0. The source of mass movement is a helix, the radius of which is equal to R_0. The helix rotates with an angular velocity ω around the axis of symmetry of the system (Fig. 1; here, the upper picture is a fragment of the reactor (Shutterstock, 2024), and the lower figures are axial and radial sections of the system). It is assumed that the helix is attached to the shafts outside the concentric reactor, or it is attached to the rotating internal shaft by heat-insulated thin spikes, the influence of which on the temperature field is neglected in the first approximation. The helix is a source of heat because it is inductively heated due to the Joule–Lenz thermoelectric effect with a constant current I. We also assume that the surfaces of the channel are thermally insulated, and the temperature boundary conditions of the 3rd kind are fulfilled at the inlet and outlet of the reactor. At the initial moment of time, the temperature of the mixture in the channel is T_0. It is necessary to calculate the temperature field at the following moments of time at an arbitrary point of the reactor, taking into account the given thermophysical, kinematic and geometric parameters of the system. For this, it is necessary to solve the inhomogeneous equation of thermal conductivity taking into account the axial velocity of the biomass medium (Carslaw and Jaeger, 1959).

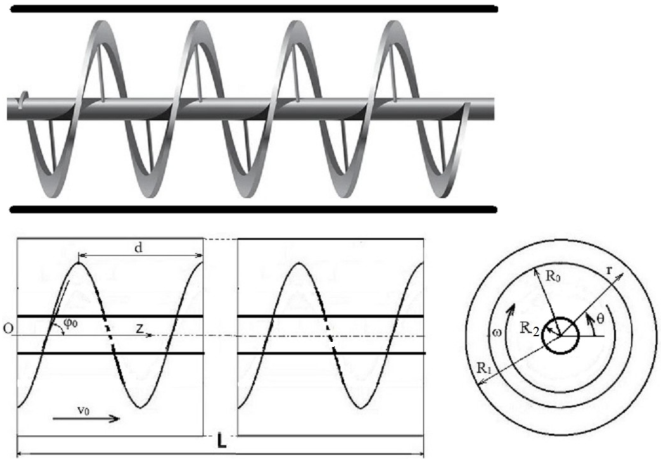

Figure 1. The scheme of a helix in a auger reactor with a rotating shaft.

$$c_p\rho\left(\frac{\partial T}{\partial \tau}+v_0\frac{\partial T}{\partial z}\right)= \lambda\left[\frac{1}{r}\frac{\partial}{\partial r}\left(r\frac{\partial T}{\partial r}\right)+\frac{1}{r^2}\frac{\partial^2 T}{\partial \theta^2}+\frac{\partial^2 T}{\partial z^2}\right]+q\left(r,\theta,z,\tau\right)$$
$$(R_2 < r < R_1, 0 < \theta < 2\pi, 0 < z < L, \tau > 0) \tag{1}$$

with an initial condition

$$T|_{\tau=0} = T_0, \tag{2}$$

the boundary conditions of thermal insulation on the lateral surfaces of the channel

$$\left.\frac{\partial T}{\partial r}\right|_{r=R_1} = 0, \tag{3}$$

$$\left.\frac{\partial T}{\partial r}\right|_{r=R_2} = 0, \tag{4}$$

and also under temperature boundary conditions of the third kind (heat exchange according to Newton's law) (Carslaw and Jaeger, 1959) at the entrance

$$\lambda\left.\frac{\partial T}{\partial z}\right|_{z=0} = -h\left(T_{\text{in}} - T|_{z=0}\right), \tag{5}$$

and exit of the channel

$$\lambda\left.\frac{\partial T}{\partial z}\right|_{z=L} = h\left(T_{\text{out}} - T|_{z=L}\right) \tag{6}$$

In these relations, r, θ, z are cylindrical coordinates with the origin point in the center of the cross section of the channel at the entrance, τ is time, h is the heat transfer coefficient; $T_0, T_{\text{in}}, T_{\text{out}}$ are the constant temperatures.

As in our previous work (Piddubniak and Ledakowicz, 2022), the body of the helix periodically rotating around the axis of the channel is replaced by continuously distributed point sources of heat, so that the intensity function $q(r,\theta,z,\tau)$ can be written in the form:

$$q(r,\theta,z,\tau) = \frac{q_0\varepsilon^2}{r\cos\varphi_0}\delta(r-R_0) \sum_{m=-\infty}^{\infty}\delta\left(\theta + 2\pi m - \frac{z\tan\varphi_0}{R_0} + \omega\tau\right), \quad (7)$$

where $\delta(x)$ is the Dirac function, $q_0 = \rho_0(jR_1)^2$, ρ_0 is the specific electric resistance of the conductor, $j = I/S$ is the electric current density, I is the current strength, S is the cross-sectional area of the helix, $\varepsilon = R_0/R_1$, φ_0 is the angle of rise of the helix.

3. METHODOLOGY FOR OBTAINING AN ANALYTICAL SOLUTION TO THE PROBLEM

Let us write the temperature T in the form of the Fourier–Bessel series

$$T(r,\theta,z,\tau) = T_{00}(z,\tau) + \sum_{m=1}^{\infty} T_{0n}(z,\tau)\,B_{0m}(r/R_1) + 2\mathrm{Re}\sum_{m=1}^{\infty}\sum_{n=1}^{\infty} T_{mn}(z,\tau)\,B_{mn}(r/R_1)\,\mathrm{e}^{-\mathrm{i}m\theta}$$
$$(R_2 < r < R_1,\ 0 < \theta < 2\pi,\ 0 < z < L,\ \tau > 0), \quad (8)$$

where

$$B_m(r/R_1) = J'_m(\mu_{mn})\,N_m(\mu_{mn}r/R_1) - N'_m(\mu_{mn})\,J_m(\mu_{mn}r/R_1) \quad (9)$$

and μ_{mn} are the roots of the transcendental equation

$$J'_m(\mu_{mn})\,N'_m(\mu_{mn}\varepsilon_0) - N'_m(\mu_{mn})\,J'_m(\mu_{mn}\varepsilon_0) = 0$$
$$(|m| = 0,1,2,\ldots;\ n = 1,2,3,\ldots). \quad (10)$$

Here $\varepsilon_0 = R_2/R_1$, $J_m(x)$ and $N_m(x)$ are, respectively, the Bessel function and the Neumann function of the mth order; the prime symbol marks the derivatives of these functions with respect to the argument, the sign Re means the real part of the complex expression.

If we introduce new functions
$\Omega_{mn}(z,\tau)$ $(|m|, n = 0,1,2,3,\ldots)$ such that

$$T_{00}(z,\tau) = \Omega_{00}(z,\tau), \quad (11)$$

$$T_{mn}(z,\tau) = P_{mn}(z,\tau)\,\Omega_{mn}(z,\tau)\times \exp\left[\mathrm{i}m\left(\frac{z\tan\varphi_0}{R_0} - \omega\tau\right)\right]$$
$$(|m| = 0,1,2,\ldots;\ n = 1,2,3,\ldots), \quad (12)$$

where

$$P_{mn}(z,\tau) = \frac{\left(1-\varepsilon_0^2\right)(\pi\mu_{mn}/2)^2 B_{mn}(\varepsilon)}{\left[1-(m/\mu_{mn})^2\right] - \left\{1-[m/(\mu_{mn}\varepsilon_0)]^2\right\}[J'_m(\mu_{mn})/J'_m(\mu_{mn}\varepsilon_0)]^2}, \quad (13)$$

then applying the integral Laplace transform over time τ (Dyke, 2004) to Equation (1) and boundary conditions (3)–(6)

$$f^{\mathrm{L}}(p) = \int_0^{\infty} f(\tau)\mathrm{e}^{-p\tau}\mathrm{d}\tau \quad (\mathrm{Re}\,p > 0), \quad (14)$$

after certain transformations we obtain inhomogeneous ordinary differential equations of the second order

$$\frac{\partial^2\Omega^{\mathrm{L}}_{mn}(z,p)}{\partial z^2} - \frac{v_m}{a}\frac{\partial\Omega^{\mathrm{L}}_{mn}(z,p)}{\partial z} - \frac{1}{a}g_{mn}(p)\,\Omega^{\mathrm{L}}_{mn}(z,p) + \frac{1}{a}\left(T_0\delta_{m0}\delta_{n0} + \frac{w}{c_p\rho}\frac{1}{p}\right) = 0$$
$$(|m|, n = 0,1,2,\ldots;\quad 0 < z < L), \quad (15)$$

with boundary conditions in transforms

$$\left[L\frac{\partial\Omega^{\mathrm{L}}_{mn}(z,p)}{\partial z} - \mathrm{Nu}^*_m\Omega^{\mathrm{L}}_{mn}(z,p)\right]_{z=0} = -\frac{1}{p}\mathrm{Nu}T_{\mathrm{in}}\delta_{m0}\delta_{n0}, \quad (16)$$

$$\left[L\frac{\partial\Omega^{\mathrm{L}}_{mn}(z,p)}{\partial z} + \mathrm{Nu}_m\Omega^{\mathrm{L}}_{mn}(z,p)\right]_{z=L} = \frac{1}{p}\mathrm{Nu}T_{\mathrm{out}}\delta_{m0}\delta_{n0}. \quad (17)$$

In relations (15)–(17) an asterisk means complex conjugation; δ_{mn} is the Kronecker symbol ($\delta_{mn} = 1$, $m = n$; $\delta_{mn} = 0$), $m \neq n$; a is the coefficient of thermal diffusivity of biomass, $a = \lambda/(c_p\rho)$ (Carslaw and Jaeger, 1959), w is the specific strength of heat source (Luikov, 1968),

$$w = \frac{q_0\varepsilon^2}{\pi R_1^2\cos\varphi_0}, \quad (18)$$

Nu is the Nusselt number, $\mathrm{Nu} = hL/\lambda$; Nu_m is the complex Nusselt number

$$\mathrm{Nu}_m = \mathrm{Nu} + i\mathrm{Nu}^i_m,$$
$$\mathrm{Nu}^i_m = m\frac{L\tan\varphi_0}{R_0} \quad (|m| = 0,1,2,\ldots), \quad (19)$$

v_m is the complex velocity of biomass movement

$$v_m = v_0\left(1 - 2\mathrm{i}m\frac{a\tan\varphi_0}{R_0 v_0}\right) \quad (|m| = 0,1,2,\ldots), \quad (20)$$

and the folowing notations are used:

$$g_{00}(p) = p, \quad g_{mn}(p) = p + \frac{a}{R_1^2}\Phi_{mn}$$
$$(|m| = 0,1,2,\ldots;\ n = 1,2,3,\ldots), \quad (21)$$

$$\Phi_{mn} = \Phi^r_{mn} + i\Phi^i_{mn} = D_{mn}\mathrm{e}^{i\varphi_{mn}},$$
$$D_{mn} = \sqrt{\Phi^{r2}_{mn} + \Phi^{i2}_{mn}}, \quad \varphi_{mn} = \arctan\left(\Phi^i_{mn}/\Phi^r_{mn}\right),$$
$$\Phi^r_{mn} = \mu^2_{mn} + \left(m\varepsilon^{-1}\tan\varphi_0\right)^2,$$
$$\Phi^i_{mn} = 2\pi m\,(1/\mathrm{Fo}_v - 1/\mathrm{Fo}_0). \quad (22)$$

Here Fo_0 are the Fourier number corresponding to the rotation period of the helix $\tau_0 = 2\pi/\omega$: $\mathrm{Fo}_0 = a\tau_0/R_1^2$. Instead, Fo_v is the Fourier number corresponding to the rotation period of a biomass particle along the helix trajectory $\tau_v = 2\pi/\omega_v$, $\omega_v = v_0 \tan\varphi_0/R_0$: $\mathrm{Fo}_v = a\tau_v/R_1^2$.

Since the free terms in the differential Equations (15) do not depend on the variable z, by performing the substitution (Luikov, 1968)

$$\Omega^{0\mathrm{L}}_{mn}(z,p) = \Omega^{\mathrm{L}}_{mn}(z,p) - \frac{1}{g_{mn}(p)}\left(T_0\delta_{m0}\delta_{n0} + \frac{w}{c_p\rho}\frac{1}{p}\right), \tag{23}$$

we obtain homogeneous ordinary differential equations of the second order with respect to functions $\Omega^{0\mathrm{L}}_{mn}(z,p)$

$$\frac{\partial^2\Omega^{0\mathrm{L}}_{mn}(z,p)}{\partial z^2} - \frac{v_m}{a}\frac{\partial\Omega^{0\mathrm{L}}_{mn}(z,p)}{\partial z} - \frac{1}{a}g_{mn}(p)\,\Omega^{0\mathrm{L}}_{mn}(z,p) = 0$$
$$(|m|, n = 0,1,2,\ldots;\ 0 < z < L), \tag{24}$$

with complicated boundary conditions

$$\left[L\frac{\partial\Omega^{0\mathrm{L}}_{mn}(z,p)}{\partial z} - \mathrm{Nu}^*_m\Omega^{0\mathrm{L}}_{mn}(z,p)\right]_{z=0} = W^{1\mathrm{L}}_{mn}(p), \tag{25}$$

$$\left[L\frac{\partial\Omega^{0\mathrm{L}}_{mn}(z,p)}{\partial z} + \mathrm{Nu}_m\Omega^{0\mathrm{L}}_{mn}(z,p)\right]_{z=L} = W^{2\mathrm{L}}_{mn}(p), \tag{26}$$

where

$$W^{1\mathrm{L}}_{mn}(p) = \frac{\mathrm{Nu}}{p}(T_0 - T_{\mathrm{in}})\,\delta_{m0}\delta_{n0} + \frac{\mathrm{Nu}^*_m}{g_{mn}(p)\,p}\frac{w}{c_p\rho},$$
$$W^{2\mathrm{L}}_{mn}(p) = -\frac{\mathrm{Nu}}{p}(T_0 - T_{\mathrm{out}})\,\delta_{m0}\delta_{n0} - \frac{\mathrm{Nu}_m}{g_{mn}(p)\,p}\frac{w}{c_p\rho}. \tag{27}$$

The general solution of Eq. (24) has the form (Korn and Korn, 2000):

$$\Omega^{0\mathrm{L}}_{mn}(z,p) = c_1\mathrm{e}^{s^+_{mn}(p)z} + c_2\mathrm{e}^{s^-_{mn}(p)z}, \tag{28}$$

where

$$s^{\pm}_{mn}(p) = \frac{v_m}{2a} \pm s_{mn}(p) \quad (|m|, n = 0,1,2,\ldots), \tag{29}$$

moreover

$$s_{00}(p) = \frac{1}{2}\sqrt{\left(\frac{v_0}{a}\right)^2 + \frac{4p}{a}},$$
$$s_{mn}(p) = \frac{1}{2}\sqrt{\left(\frac{v_m}{a}\right)^2 + \frac{4}{a}g_{mn}(p)}$$
$$(|m| = 0,1,2,\ldots;\ n = 1,2,3,\ldots). \tag{30}$$

Then, satisfying the boundary conditions (25) and (26), we obtain the following system of algebraic equations for determining the coefficients c_1 and c_2:

$$a^{11}_{mn}(p)\,c_1 + a^{12}_{mn}(p)\,c_2 = W^{1\mathrm{L}}_{mn}(p),$$
$$a^{21}_{mn}(p)\,c_1\mathrm{e}^{s^+_{mn}(p)L} + a^{22}_{mn}(p)\,c_2\mathrm{e}^{s^-_{mn}(p)L} = W^{2\mathrm{L}}_{mn}(p), \tag{31}$$

where

$$a^{11}_{mn}(p) = \frac{Lv_0}{2a} + s_{mn}(p)\,L - \mathrm{Nu},$$
$$a^{12}_{mn}(p) = \frac{Lv_0}{2a} - s_{mn}(p)\,L - \mathrm{Nu},$$
$$a^{21}_{mn}(p) = \frac{Lv_0}{2a} + s_{mn}(p)\,L + \mathrm{Nu},$$
$$a^{22}_{mn}(p) = \frac{Lv_0}{2a} - s_{mn}(p)\,L + \mathrm{Nu}. \tag{32}$$

Solving this system of equations and substituting the found coefficients c_1 and c_2 in (28), taking into account notations (21) and (27), we find the solution to the problem in the Laplace transforms:

$$\Omega^{0\mathrm{L}}_{mn}(z,p) = \frac{\mathrm{Nu}}{pd^0_{00}(p)}\Big\{(T_0 - T_{\mathrm{in}})\,d^1_{00}(z,p)\,\mathrm{e}^{\frac{v_0z}{2a}} -$$
$$- (T_0 - T_{\mathrm{out}})\,d^2_{00}(z,p)\,\mathrm{e}^{-\frac{v_0(L-z)}{2a}} +$$
$$+ \frac{w}{c_p\rho p}\left[d^1_{00}(z,p)\,\mathrm{e}^{\frac{v_0z}{2a}} - d^2_{00}(z,p)\,\mathrm{e}^{-\frac{v_0(L-z)}{2a}}\right]\Big\}\,\delta_{m0}\delta_{n0} +$$
$$+ \frac{w}{c_p\rho p_{mn}}\frac{d^3_{mn}(z,p)}{d^0_{mn}(p)}\left(\frac{1}{p} - \frac{1}{p + p_{mn}}\right)(1 - \delta_{n0})$$
$$(0 < z < L;\quad |m|,\ n = 0,1,2,\ldots), \tag{33}$$

where

$$p_{mn} = \frac{a}{R_1^2}\Phi_{mn}, \tag{34}$$

$$d^0_{mn}(p) = a^{12}_{mn}(p)\,a^{21}_{mn}(p)\,\mathrm{e}^{s_{mn}(p)L} -$$
$$- a^{11}_{mn}(p)\,a^{22}_{mn}(p)\,\mathrm{e}^{-s_{mn}(p)L},$$
$$d^1_{mn}(z,p) = a^{21}_{mn}(p)\,\mathrm{e}^{s_{mn}(p)(L-z)} -$$
$$- a^{22}_{mn}(p)\,\mathrm{e}^{-s_{mn}(p)(L-z)},$$
$$d^2_{mn}(z,p) = a^{12}_{mn}(p)\,\mathrm{e}^{s_{mn}(p)z} - a^{11}_{mn}(p)\,\mathrm{e}^{-s_{mn}(p)z},$$
$$d^3_{mn}(z,p) = \mathrm{Nu}^*_m d^1_{mn}(z,p)\,\mathrm{e}^{\frac{v_mz}{2a}} -$$
$$- \mathrm{Nu}_m d^2_{mn}(z,p)\,\mathrm{e}^{-\frac{v_m(L-z)}{2a}}. \tag{35}$$

Applying the inverse formula of the Laplace integral transform (Dyke, 2004)

$$f(\tau) = \frac{1}{2\pi i}\int_{\sigma-i\infty}^{\sigma+i\infty} f^{\mathrm{L}}(p)\mathrm{e}^{p\tau}\,dp \quad (\sigma > 0), \tag{36}$$

based on Eq. (23), we obtain the following result:

$$\Omega_{mn}(z,\tau) = \left(T_0 + \frac{w}{c_p\rho}\tau\right)\delta_{m0}\delta_{n0} +$$
$$+ \frac{w}{c_p\rho p_{mn}}\left(1 - \mathrm{e}^{-p_{mn}\tau}\right)(1 - \delta_{n0}) + \Omega^0_{mn}(z,\tau)$$
$$(0 < z < L,\quad \tau > 0;\quad |m|,\ n = 0,1,2,\ldots). \tag{37}$$

We can obtain the inversion formula for the function $\Omega^{0\mathrm{L}}_{mn}(z,p)$ approximately by using the fact that the parameter $\alpha = a(Lv_0)^{-1}$ is small (in specific cases of the order of 10^{-4}) (Ledakowicz and Piddubniak, 2023). If, in addition, dimensionless variables and parameters are used

$$\begin{aligned}&\xi = r/R_1, \quad \zeta = z/L, \quad \mathrm{Fo} = a\tau/R_1^2,\\ &\beta = R_1/L, \quad \gamma = 2\alpha/\beta = 2a/(R_1 v_0),\end{aligned} \tag{38}$$

where Fo is the Fourier number, then finally the expression for the temperature can be formally written in the form

$$\begin{aligned}&T(\xi,\theta,\zeta,\mathrm{Fo}) = T_{00}(\zeta,\mathrm{Fo}) + \sum_{n=1}^{\infty} T_{0n}(\zeta,\mathrm{Fo})\, B_{0n}(\xi) +\\ &+ 2\mathrm{Re}\sum_{m=1}^{\infty}\sum_{n=1}^{\infty} T_{mn}(\zeta,\mathrm{Fo})\, B_{mn}(\xi)\, \mathrm{e}^{-\mathrm{i}m\theta}\\ &(\varepsilon_0 < \xi < 1,\ 0 < \theta < 2\pi,\ 0 < \zeta < 1,\ \mathrm{Fo} > 0).\end{aligned} \tag{39}$$

where

$$\begin{aligned}&T_{00}(\zeta,\mathrm{Fo}) \approx T_0 - \Big[(T_0 - T_{\mathrm{in}})\, R_{00}^1(z) +\\ &\quad + (T_0 - T_{\mathrm{out}})\, R_{00}^2(\zeta) + \frac{q_0}{\pi\lambda\cos\varphi_0} c_{00} R_{00}^3(\zeta)\Big] \times\\ &\quad \times \left(1 - \mathrm{e}^{-\mathrm{Fo}\gamma^{-2}}\right) \quad (0 < \zeta < 1, \quad \mathrm{Fo} > 0),\end{aligned} \tag{40}$$

$$\begin{aligned}&T_{0n}(\zeta,\mathrm{Fo}) \approx \frac{q_0}{\pi\lambda\cos\varphi_0} c_{0n} \times\\ &\quad \times \left[1 + 2\alpha R_{0n}^3(\zeta)\right]\left[1 - \mathrm{e}^{-\left(\mu_{0n}^2 + \gamma^{-2}\right)\mathrm{Fo}}\right]\\ &\quad (0 < \zeta < 1, \quad \mathrm{Fo} > 0; \quad n = 1,2,3,\ldots),\end{aligned} \tag{41}$$

$$\begin{aligned}&2\mathrm{Re}\left[T_{mn}(\zeta,\mathrm{Fo})\mathrm{e}^{-im\theta}\right] \approx \frac{q_0}{\pi\lambda\cos\varphi_0} c_{mn} \times\\ &\times \Big\langle \left[K_{mn}^r(\zeta) + 2\alpha R_{mn}^{3r}(\zeta)\right] \times\\ &\times \left\{\cos\left[m\left(\theta + 2\pi\mathrm{Fo}/\mathrm{Fo}_0\right)\right] - \cos(m\theta)\, \mathrm{e}^{-\left(\mu_{mn}^2 + \gamma^{-2}\right)\mathrm{Fo}}\right\} -\\ &- \left[K_{mn}^i(\zeta) + 2\alpha R_{mn}^{3i}(\zeta)\right] \times\\ &\times \left\{\sin\left[m\left(\theta + 2\pi\mathrm{Fo}/\mathrm{Fo}_0\right)\right] - \sin(m\theta)\, \mathrm{e}^{-\left(\mu_{mn}^2 + \gamma^{-2}\right)\mathrm{Fo}}\right\}\Big\rangle\\ &(0 < \zeta < 1, \quad \mathrm{Fo} > 0; \quad m,n = 1,2,3,\ldots).\end{aligned} \tag{42}$$

Note that in the case where $T_{\mathrm{in}} = T_{\mathrm{out}} = T_c$, Eq. (40) takes the form:

$$\begin{aligned}&T_{00}(z,\tau) \approx T_0 + \left[T_c - T_0 - \frac{q_0}{\pi\lambda\cos\varphi_0} c_{00} R_{00}^3(\zeta)\right] \times\\ &\times \left(1 - e^{-\mathrm{Fo}\gamma^{-2}}\right) \quad (0 < \zeta < 1, \quad \mathrm{Fo} > 0),\end{aligned} \tag{43}$$

because $R_{0n}^1(\zeta) + R_{0n}^2(\zeta) = 1$.

The explicit form of the coefficients and functions from these relations is given in Appendix.

4. SPECIFIC CALCULATIONS OF THE TEMPERATURE FIELD IN A CONCENTRIC CHANNEL OF FINITE LENGTH

With an exact solution to the problem, it is possible to perform a numerical calculation of the temperature in a channel containing a moving aggregate (pseudo-liquefied biomass) in a given situation. To this end, we will select system parameters that mirror the parameters observed during the experimental research (Nachenius et al., 2015b; Shi et al., 2019), as summarized in Table 1.

Note that with the selected channel length, the Nusselt number is Nu = 46.86. The dimensionless radii of the helix and shaft are respectively $\varepsilon = 0.962$ and $\varepsilon_0 = 0.346$. Similarly, given the velocity of biomass movement in the axial direction of the cylindrical channel, we obtain $\mathrm{Fo}_v = 0.593$, and with the above given angular velocity of the helix, we find $\mathrm{Fo}_0 = 0.0135$. Assuming the helix is made of tungsten, then the constant q_0, which is included in the heat intensity function (7), will be equal to $q_0 = 18.40$ W/m. For the specific power of the heat source, the value will be $w = 2.850 \cdot 10^4$ W/m^3.

Based on calculations according to Eqs. (41)–(43), Fig. 2a illustrates the temperature distribution as a function of the Fourier number Fo at the point $\xi = 0.5$, $\theta = 0°$, $\zeta = 0.8$ for different values of the current strength I and at $R_2 = 0.009$ m ($\varepsilon_0 = 0.346$). Fig. 2b shows similar results, for $R_2 = 0.018$ m ($\varepsilon_0 = 0.692$). Here $R_0 = 0.025$ m ($\varepsilon = 0.962$). We calculated the roots μ_{mn} of the transcendental Equation (10) using the "regula falsi" method (Pflanz, 1948). A logarithmic scale is used for the time coordinate. A rather short transient process of the order of Fo ≈ 0.015, corresponding to a time constant of approximately $\tau \approx 24$ s, is clearly visible. After that, the temperature reaches a long-term quasi-stationary regime. Fig. 2 also shows, that in the quasi-stationary mode the temperature reaches the level of approximately $T = 356$ K for $R_2 = 0.009$ m and $T = 395$ K for $R_2 = 0.018$ m when a current strength of $I = 5$ A is chosen. However, the quasi-stationary temperature is also characterized by a microstructure that has an oscillating character and depends on the angular velocity (cyclic frequency) of the helix's the rotation and its geometric dimensions.

Figure 3a shows a fragment of the temperature change over a short period of time (incomplete four revolutions of the helix) at the point $\xi = 0.8$, $\theta = 0°$, $\zeta = 0.5$ at $I = 5$ A and $\varepsilon = 0.961$. Similar results are presented in Fig. 3b, but with $\varepsilon = 0.481$ (the radius of the helix is two times smaller). Here $\varepsilon_0 = 0.346$. At the micro-level, the temperature signal takes the form of amplitude-modulated oscillations with a period of Fo_0 =0.0135. This cyclicity is clearly related to the helix's rotation frequency, while the quasi-regularity of the amplitude within one period of the signal is related to the phenomenon of re-reflection of heat flows from the reactor's cylindrical surfaces, as well as its input and output impedance surfaces. At the same time, the amplitude of temperature oscillations at this point is quite small, at around 0.42 K.

Despite the oscillatory temperature components related to the geometric and kinematic parameters of the helix being quite weak against the background of the general temperature field, it is advisable to analyse them in more detail. To this end, we will focus on the part of the temperature that depends only on the volumetric heat source, i.e. the one containing the specific power of the heat source *w*, using the following function:

$$\vartheta(\xi,\theta,\zeta,Fo) = \Big[T(\xi,\theta,\zeta,Fo) - T_0 - (T_c - T_0)\times \\ \times\left(1 - e^{-\mathrm{Fo}/\gamma^2}\right)\Big] / [q_0/(\pi\lambda)], \qquad (44)$$

which we will call the sensitivity function. Here $T_c = T_{\mathrm{in}} = T_{\mathrm{out}} = 300$ K. Under the selected thermophysical parameters $q_0/(\pi\lambda) \approx 17$ K.

Figure 4 demonstrates the change of this function over three oscillation periods at points located along the ray $0 < \xi < 1$, $\theta = 0°$ in the middle cross-section of the reactor $\zeta = 0.5$. Fig. 4a refers to the case when the helix radius is equal to $\varepsilon = 0.961$, and Fig. 4b refers to the case when the helix radius is half that, i.e. $\varepsilon = 0.482$. Here $\varepsilon_0 = 0.346$ again. As can be seen from these figures, the temperature amplitude increases sharply when the helix is closest to the observation point. Similar, but much weaker, temperature amplitude spikes occur for a screw of finite width when its crest passes near the observation point (Piddubniak and Ledakowicz, 2022).

Table 1. Geometric, kinematic and thermophysical parameters of the process.

Parameter	Symbols	Units	Values
Density of biomass	ρ	kg/m^3	551
Heat capacity of biomass	c_p	J/(kg·K)	1502
Coefficient of thermal conductivity	λ	W/(m·K)	0.35
Thermal diffusivity of biomass	a	m^2/s	$4.23 \cdot 10^{-7}$
Initial temperature of biomass	T_0	K	293.15
Temperature at channel entry	T_{in}	K	300
Temperature at channel exit	T_{out}	K	300
Surface heat transfer coefficient	h	W/(m^2·K)	10
Reactor length	L	m	1.64
Radius of channel	R_1	m	0.026
Radius of shaft	R_2	m	0.009
Radius of helix	R_0	m	0.025
Velocity of biomass movement	v_0	m/s	$5.888 \cdot 10^{-4}$
Angular velocity of helix	ω	Hz	0.292
Angle of helix inclination	φ_0	°	73.68
Helix pitch	$d = 2\pi R_0 \mathrm{ctan}\varphi_0$	m	0.046
Radius of helix cross-section	r_0	m	$1.5 \cdot 10^{-3}$
Electrical resistance of helix material	ρ_0	Ohm	$4.44 \cdot 10^{-8}$

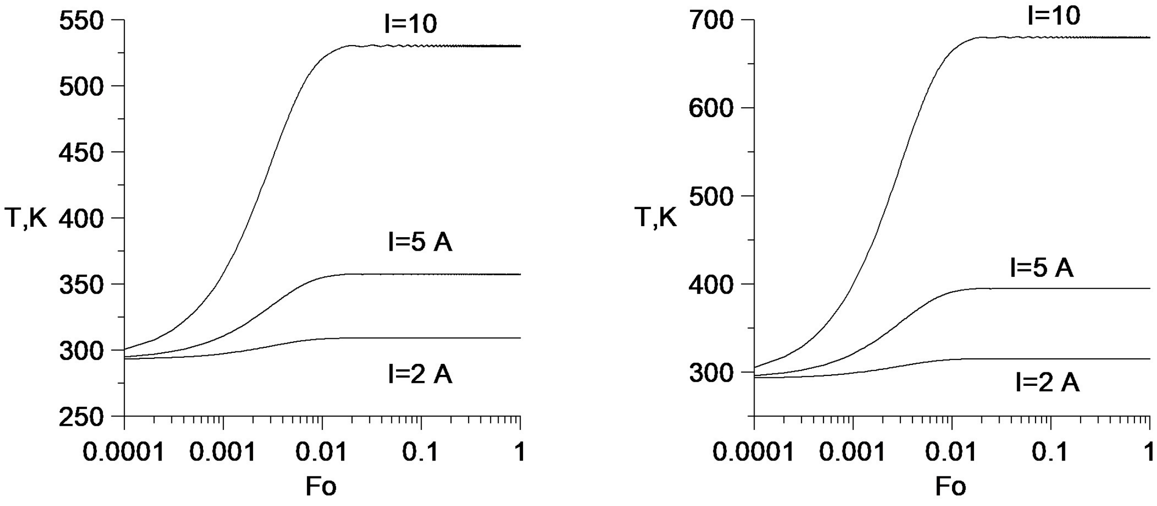

(a) (b)

Figure 2. Temperature as a function of the Fourier number Fo at the point $\xi = 0.8$, $\theta = 0°$, $\zeta = 0.5$ for different values of the current strength I and $\varepsilon = 0.025$ (a – $\varepsilon_0 = 0.346$; b – $\varepsilon_0 = 0.692$).

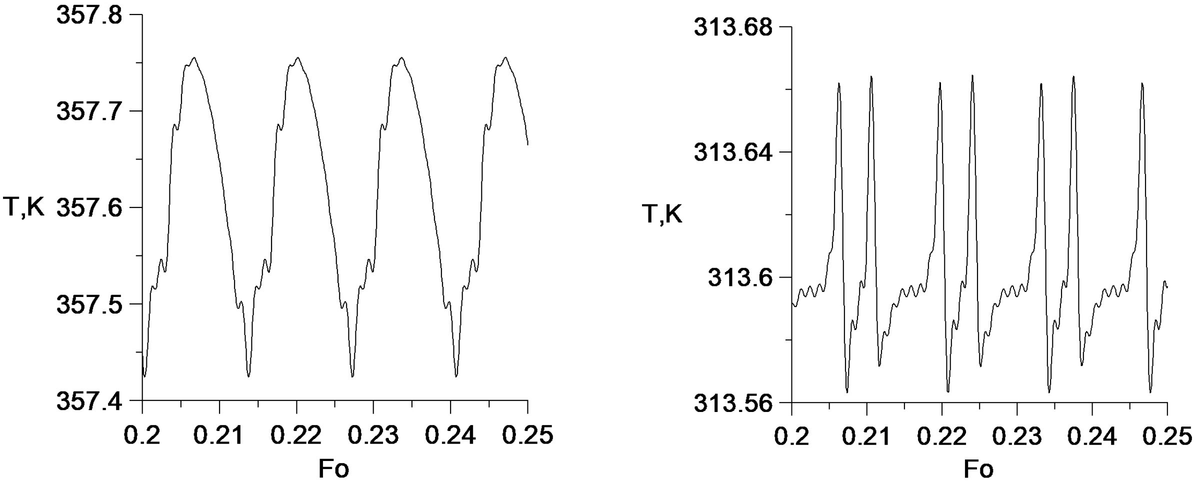

(a) (b)

Figure 3. The fragments of the temperature profile at the point $\xi = 0.8$, $\theta = 0°$, $\zeta = 0.5$ for $I = 5$ A and $\varepsilon_0 = 0.346$ (a – $\varepsilon = 0.962$; b – $\varepsilon = 0.481$).

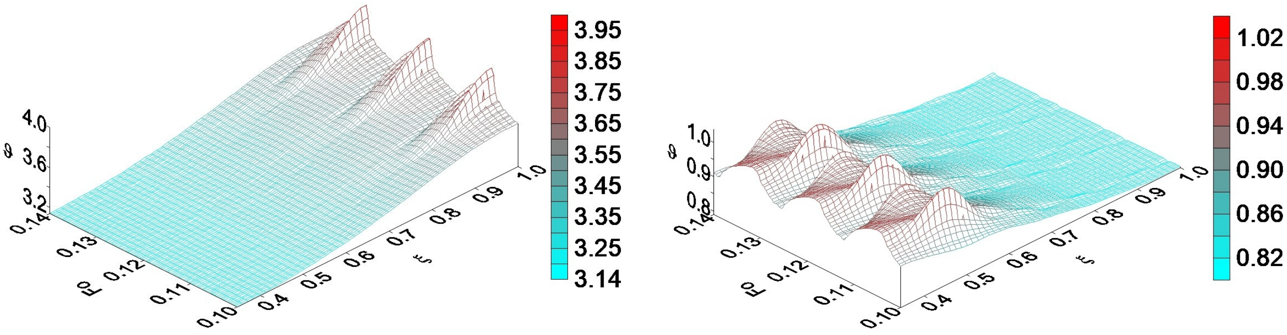

(a) (b)

Figure 4. Time variation of the sensitivity function ϑ on the ray $0 \le \xi \le 1$, $\theta = 0°$, $\zeta = 0.5$ for the three periods of microoscillation and with $\varepsilon_0 = 0.346$ (a – $\varepsilon = 0.962$; b – $\varepsilon = 0.481$).

Fig. 5 shows how the sensitivity function ϑ changes over time for points located on a circle with a radius of $\xi = 0.8$ and $0 \le |\theta| \le 180°$, in the middle cross section of the reactor $\xi = 0.8$, $0 \le |\theta| \le 180°$, $\zeta = 0.5$. In this case, the relative radii of the helix and the shaft are equal, ($\varepsilon = 0.962$ and $\varepsilon_0 = 0.346$, respectively) and the observation period spans three rotations of the heat source. The graph clearly reproduces the geometric structure of the helix. Notably, the amplitude of the maximum temperature values, which are positioned at an angle of $\pi/2 - \varphi_0$ to the angular coordinate axis of the channel, remains virtually unchanged along the ridges of the helix. At the same time, the cross-section of these amplitudes is modulated (see also Fig. 3), which is associated with heat superposition processes on the concentric surfaces of the reactor.

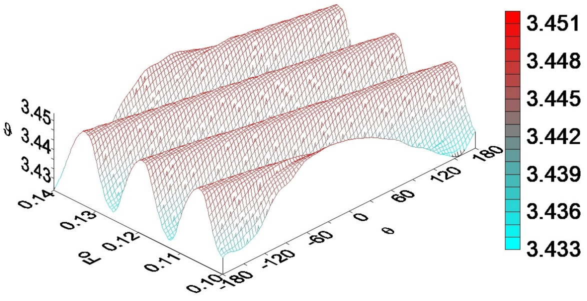

Figure 5. The time dependence of the function ϑ on the circle $\xi = 0.8$, $0 \le |\Theta| \le 180°$, $\zeta = 0.5$ for the three periods of the helix rotation, when $\varepsilon = 0.962$ and $\varepsilon_0 = 0.346$.

Figures 6a and 6b show the periodic structure of the function ϑ over time, along a short section of the reactor's axis at the point where $\xi = 0.8$, $\theta = 0°$, $0.2 < \zeta < 0.3$. Here, $\varepsilon = 0.962$ and $\varepsilon_0 = 0.346$. Fig. 6a shows that amplitude of the sensitivity function increases in the axial direction of the channel with slight fluctuations from the entrance to the exit. A similar phenomenon was observed in theoretical and experimental works (Luz et al., 2017; Luz et al., 2018; Morgano, 2019; Nachenius et al., 2015a; Rego, 2021; Sanchís et al., 2022; Shi et al., 2019; Teo et al., 2018), albeit not to such a quantitative extent. Fig. 6b illustrates the microstructure of the oscillations obtained when the $T_{00}(\zeta, \mathrm{Fo})$ contribution is not taken into account. This takes the form of standing heat waves with helical amplitudes, the maxima of which correspond to the moments when the helix crest approaches the observation point. The normals to the fronts of these waves are inclined at an angle φ_0 to the reactor axis. The instantaneous (Fo = 0.5) three-dimensional dependence of the sensitivity function on the coordinates ξ and θ in the middle cross-section of the reactor $\zeta = 0.5$ is shown in Fig. 7a and Fig. 7b for $\varepsilon_0 = 0.346$ and $\varepsilon_0 = 0.692$, respectively. In both cases $\varepsilon = 0.962$. As can be seen, the temperature changes slightly in the angular direction against the background of an intense change in the radial direction. Notably, significant temperature amplitude maxima in the angular direction are only reached at points near the helix.

Fig. 8a and Fig. 8b ($\varepsilon = 0.962$ and $\varepsilon = 0.481$, respectively) likely depict the instantaneous changes in the sensitivity function in the (ξ, ζ) plane over a small interval along the axial variable, $0.2 < \zeta < 0.3$, when $\varepsilon_0 = 0.692$. The temperature microfield maxima are visible in the form of ridges here, the spacing of which which is equal to the dimensionless pitch of the helix $d/L = 0.028$.

Fig. 9a shows the instantaneous distribution of the sensitivity function in the $(\theta,\ \zeta)$ plane, while Fig. 9b shows the same distribution without the $T_{00}(\zeta,\ \mathrm{Fo})$ contribution. Here and further $\varepsilon = 0.962$, $\varepsilon_0 = 0.692$. Due to the superposition of heat flows along the spiral ridges of heat propagation, it can be seen that a quasi-periodic temperature structure occurs in the axial $\theta =$const and azimuthal $\zeta =$ const cross-sections.

The phenomenon of space-time resonance was also observed in finite-length reactors (Ledakowicz and Piddubniak, 2023) and infinite reactors (Ledakowicz and Piddubniak, 2021).This is characterized by a local increase in the sensitivity function ϑ when the screw's rotation frequency reaches a certain value associated with the velocity of the fluidized mass flow v_0, under the condition of space-time synchronism using the equation $\mathrm{Fo}_v = \mathrm{Fo}_0$, or $v = R_0\omega = v_0 \tan\varphi_0$. This

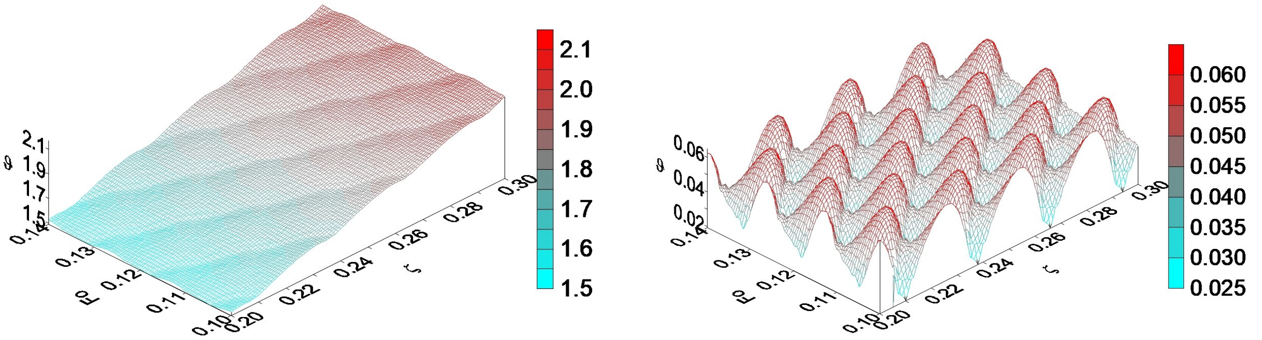

(a) (b)

Figure 6. The time dependence of the function ϑ (Fig. 6b without the contribution of the background component T_{00}) on at interval $0.2 \le \zeta \le 0.3$ for $\xi = 0.8$, $\theta = 0°$, $\varepsilon = 0.962$, $\varepsilon_0 = 0.346$ and for the three periods of oscillation.

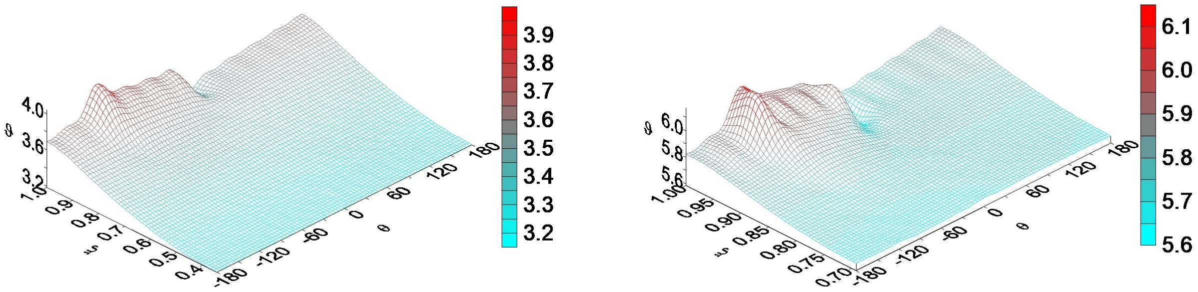

(a) (b)

Figure 7. The 3-D radial-angular distribution of the function ϑ in the middle cross-section $\zeta = 0.5$ for $\mathrm{Fo} = 0.5$, $\varepsilon = 0.962$ ($a - \varepsilon_0 = 0.346$; $b - \varepsilon_0 = 0.692$).

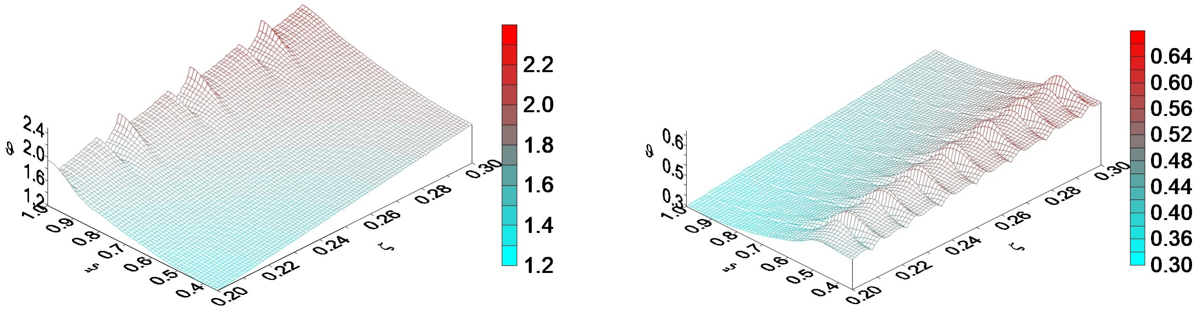

(a) (b)

Figure 8. The radial-axial distribution of the function ϑ in the plane $0 \le \xi \le 1$, $0.2 \le \zeta \le 0.3$ for $\theta = 0°$, $\mathrm{Fo} = 0.5$, $\varepsilon_0 = 0.692$ ($a - \varepsilon = 0.962$; $b - \varepsilon = 0.481$).

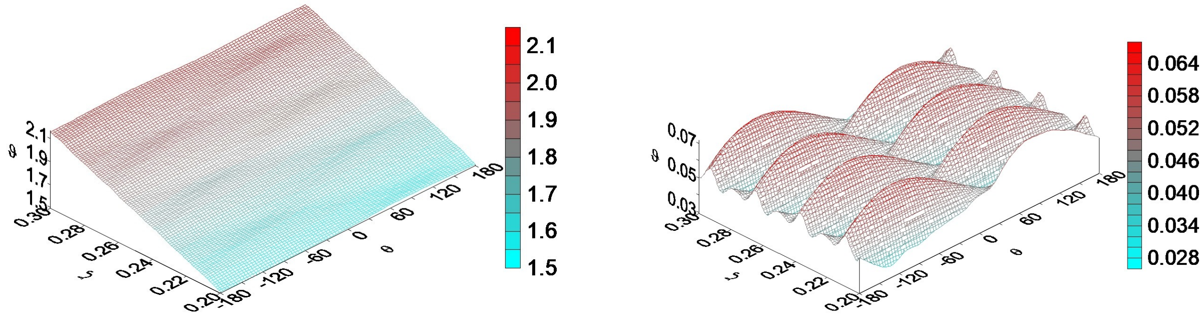

(a) (b)

Figure 9. The 3-D axial-angular distribution of function ϑ (Fig. 9b without the T_{00} contribution) for Fo $= 0.5$ on the cylindrical surface $\xi = 0.8$, $0 \le |\theta| \le 180°$, $0.2 \le \zeta \le 0.3$.

universal phenomenon also occurs in the case. This is illustrated in Fig. 10. Calculations were performed at the point $\xi = 0.8$, $\theta = 0°$, $\zeta = 0.5$ at the moment when Fo $= 0.5$ and $v_0 = 5.89 \cdot 10^{-4}$ m/s ($\varphi_0 = 73.68°$, $\text{Fo}_v = 0.593$). The peak of the maximum amplitude occurs at the value of $\omega = \omega_{\text{res}} \approx 0.085$ Hz, with the difference in the function ϑ reaching a value of 1.24.

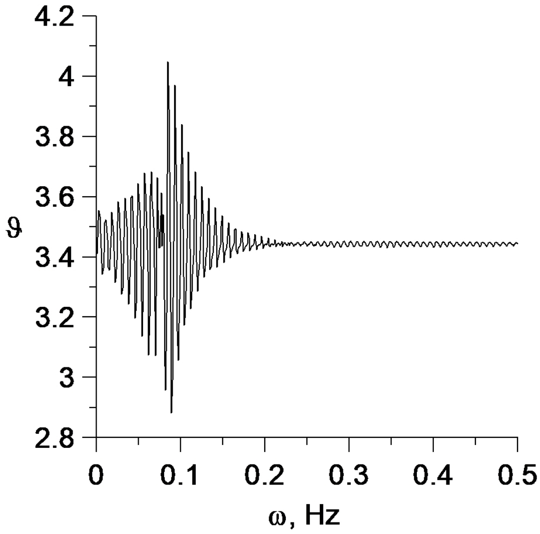

Figure 10. Transition of the function ϑ through resonance at the point $\xi = 0.8$, $\theta = 0°$, $\zeta = 0.5$ for Fo $= 0.5$, $\varphi_0 = 73.68°$ and $v_0 = 5.89 \cdot 10^{-4}$ m/s ($\text{Fo}_v = 0.593$).

With a constant screw rotation frequency of $\omega = 0.292$ Hz ($\text{Fo}_0 = 0.0135$), and a variable mixture movement velocity v_0, the velocity is maintained at the value at which the sensitivity function amplitude ϑ reaches an extreme value and its phase changes sharply. From the calculations illustrated in Fig. 11 for the case when $T_{00}(\zeta, \text{Fo})$ is not taken into account and the following values are used: $\xi = 0.8$, $\theta = 0°$, $\zeta = 0.5$, Fo $= 0.5$, $\varphi_0 = 73.68°$, it appears that the phase change is obtained at $v_0 = v_{0\text{res}} \approx 0.00202$ m/s. From the condition of space-time synchronism, the angular velocity of the screw is found to be $\omega \approx v_0 \tan \varphi_0 / (R_0 \varepsilon) = 0.288$ Hz, for this case, indicating that this condition is fulfilled quite accurately.

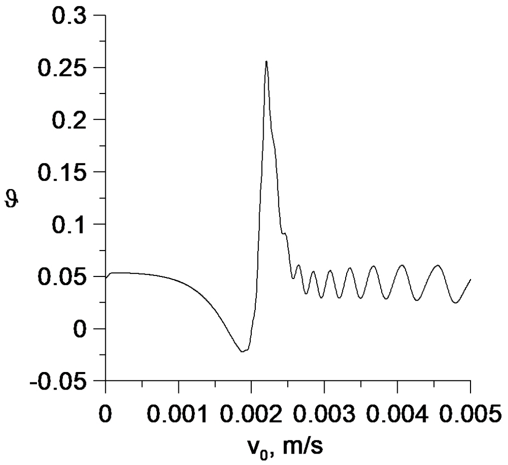

Figure 11. Dependence of the influence function ϑ (without the T_{00} contribution) on the velocity of biomass movement v_0 at the point $\xi = 0.8$, $\theta = 0°$, $\zeta = 0.5$ for Fo $= 0.5$, $\varphi_0 = 73.68°$, $\omega = 0.292$ Hz.

From the calculations, we also find that for a velocity of biomass movement of $v_0 = v^* = 0.512 \cdot 10^{-4}$ m/s for different values of the dimensionless variable ζ, on the straight line $\xi = 0.8$, $\theta = 0°$ and at $\varphi_0 = 73.68°$, with a current strength $I = 1$ A, the temperature rises sharply locally (Fig. 12). As Equations (43), (A.2) show, this is due to the product

$$\alpha \left(1 - e^{-\text{Fo}/\gamma^2}\right) = \alpha \left[1 - e^{-\beta^2 \text{Fo}/(2\alpha)^2}\right] \tag{45}$$

at a fixed Fourier number Fo (Fo $= 0.5$ in this case). At the same time, the parameter α remains small, $\alpha = 0.00504$. As the movement of the biomass is caused by the rotation of the helix, it follows from the condition of spatio-temporal synchronism $\omega = v_0 \tan \varphi_0 / (R_0 \varepsilon)$ that this velocity should correspond to the frequency of helix's rotation ($\omega = 0.0073$ Hz) with the system's geometric parameters remaining unchanged.

The velocity of biomass movement does not remain constant throughout the entire heating time interval. Fig. 13 illustrates this, showing the dependence of the total temperature T on the velocity v_0 and the Fourier number Fo obtained at the point $\xi = 0.8$, $\theta = 0°$, $\zeta = 0.5$ for $\varphi_0 = 73.68°$, $\omega = v_0 \tan\varphi_0/(R_0\varepsilon)$ and for the current $I = 1$ A. As can be seen at a fixed velocity of biomass movement, the maximum temperature value in the transition mode is only reached for a specific Fourier number value. In other words the extreme velocity value $v_0 = v_0^*$ disperses over time.

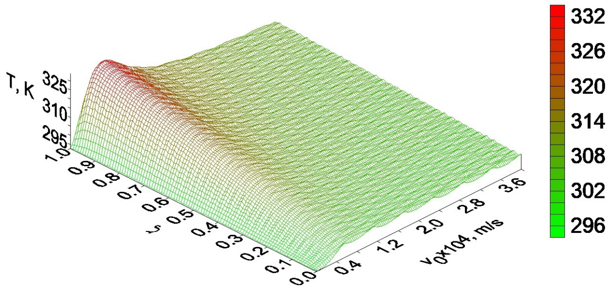

Figure 12. Local increase of the temperature T near the value $v_0 = 0.512 \cdot 10^{-4}$ m/s for different values of the dimensionless variable $\zeta, 0 \le \zeta \le 1$, on the straight line $\xi = 0.8$, $\theta = 0°$ and for $\mathrm{Fo} = 0.5$, $\varphi_0 = 73.68°$, $\omega = 0.0073$ Hz.

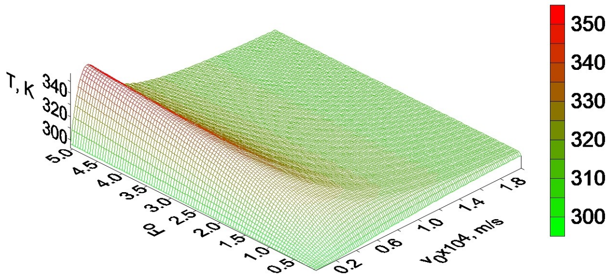

Figure 13. Dependence of the temperature T on the velocity v_0 and the Fourier number Fo at the point $\xi = 0.8$, $\theta = 0°$, $\zeta = 0.5$ for $\varphi_0 = 73.68°$, $\omega = v_0 \tan\varphi_0/(R_0\varepsilon)$ and the current $I = 1$ A.

This dispersion relationship can be determined by re-examining the multiplier (45). Let us consider a function

$$f(x) = x\left(1 - e^{-1/x^2}\right), \quad x = \frac{\alpha}{\beta\sqrt{\mathrm{Fo}}} = \frac{a}{v_0 R_1 \sqrt{\mathrm{Fo}}}, \tag{46}$$

where notation (38) is taken into account. The maximum value of this function is obtained at $x \approx 0.892$. Then

$$v_0^* \approx 1.121 \frac{a}{R_1\sqrt{\mathrm{Fo}}}, \tag{47}$$

On the other hand, if the velocity of mass movement is fixed, then the critical Fourier number near which a local temperature increase occurs is determined by the formula

$$\mathrm{Fo} = \mathrm{Fo}^* \approx 1.257 \left(\frac{\mathrm{a}}{\mathrm{v_0 R_1}}\right)^2. \tag{48}$$

Note that the Fourier number, which determines the duration of the temperature transient process, is proportional to the parameter $a^2/(v_0 R_1)^2$. In other words, the faster the mass movement velocity, the shorter the transient process.

5. SUMMARY AND CONCLUSIONS

Some auger pyrolyzer designs have a very small screw width, which is particularly important when processing viscous and sticky materials, such as biomass. This study presents a new mathematical model for heating biomass in a concentric cylindrical channel of finite length. A spiral mounted on a shaft is the source of the heat and the means by which the biomass moves. This spiral uses induction heating based on the Joule–Lenz effect and rotates around its own axis. Let us summarize the results of the calculations and compare them with those obtained for a wide-shafted screw (Ledakowicz and Piddubniak, 2023).

- In both cases, the exact solution to the problem is obtained in the form of a Fourier–Bessel series. However, the coefficients of the helix series are obtained explicitly, while the coefficients of the wide screw series are obtained via quadratures, which are calculated approximately.
- Numerical analysis shows that the transient temperature field process is very short-lived, on the order of $a^2/(v_0 R_1)^2$ after which the temperature reaches a quasi-stationary regime. Significant differences associated with the type of screw are observed in the fine structure of the temperature field during the heater's quasi-monochromatic operating mode.
- The quasi-stationary part of the temperature field is characterised by amplitude-modulated oscillations against a constant temperature background. The frequency of these oscillations is determined by the auger or helix's rotation period.
- As has been noted by other researchers the temperature increases along the channel axis in the direction of biomass movement.
- There are significantly larger temperature oscillation amplitudes than in the case of a wide screw. Additionally, the sensitivity function amplitude level depends significantly on the helix's location: the closer the helix is to the outer surface of the channel, the higher the level.
- Modulations of the temperature field in the axial and azimuthal directions are most clearly observed, where the temperature distribution is sensitive to the helix's geometry and rotation frequency. This is a consequence of the complex superposition of heat flows that are reflected from the ends of the reactor.
- The phenomenon of resonant amplification of the sensitivity function depending on the screw rotation frequency is revealed. This occurs under the conditions of space-time synchronism described in the work. This effect is more pronounced with a helix than with a wide screw.
- A similar resonance phenomenon occurs when the speed of the biomaterial's movement changes. This phenomenon is more pronounced with a helix than with a wide screw. Under conditions of spatiotemporal synchronism, a resonant change in the phase of the sensitivity function is obtained.
- It was established that in regions of very low biomass movement velocities, an extreme increase in temperature ampli-

tude occurs. This phenomenon is described by the "piston" model of the temperature field, which is closely related to the small parameter of the problem. This model is characterized by an increase in temperature along the reactor from the inlet to the outlet. These extreme changes in temperature amplitude at fixed low biomass velocities occur at times inversely proportional to the square of the velocity.

It should be emphasized that the presented analysis of the temperature field is only the first step in solving a more general problem: mathematically modeling the biomass pyrolysis process using interconnected heat and mass transfer equations that account for the heat of exothermic reactions. Further investigation should focus on verifying the temperature distribution inside the screw reactor or sterilizer through experimentation. This would allow us to explore the possibility of optimizing the heating process by varying the electric current and the frequency of the helix's rotation. In the context of industrial applications of biomass waste pyrolysis, this relates to energy savings. Conversely, for the sterilization of herbs, spices, and flavorings, it is necessary to provide controlled temperature conditions to avoid charring.

A. APPENDIX STRUCTURE COEFFICIENTS AND FUNCTIONS IN EXPRESSIONS FOR TEMPERATURE COMPONENTS

The Eqs. (40)–(42) contain the coefficients

$$\begin{aligned}
&c_{00} = \frac{\varepsilon^2\alpha}{\beta^2\left(1-\varepsilon_0^2\right)},\\
&c_{mn} = \frac{\varepsilon^2\,(\pi/2)^2\left(\mu_{mn}^2/D_{mn}\right)B_{mn}(\varepsilon)}{1-(m/\mu_{mn})^2-\left\{1-\left[m/(\mu_{mn}\varepsilon_0)\right]^2\right\}\left[J'_m(\mu_{mn})/J'_m(\mu_{mn}\varepsilon)\right]^2}\\
&(m=0,1,2,3,\ldots;\quad n=1,2,3,\ldots)\,.
\end{aligned}\tag{A.1}$$

The functions $R_{00}^1(\zeta)$ and $R_{00}^2(\zeta)$ have the physical nature of the reradiation coefficients of the axisymmetric heat flow of the piston type from the input $\zeta=0$ and output $\zeta=1$ channel cross-sections, respectively, and $R_{00}^3(\zeta)$ are a combination of these coefficients, for which the following formulas are fulfilled:

$$\begin{aligned}
&R_{00}^1(\zeta) = \frac{d_{00}^1(\zeta)}{d_{00}^0},\\
&R_{00}^2(\zeta) = \frac{d_{00}^2(\zeta)}{d_{00}^0}\mathrm{e}^{-(1-\zeta)\alpha^{-1}},\\
&R_{00}^3(\zeta) = \frac{1}{\mathrm{Nu}}\frac{d_{00}^3(\zeta)}{d_{00}^0},\\
&d_{00}^0 = 1+\alpha\mathrm{Nu}+(1-\alpha\mathrm{Nu})\,\mathrm{e}^{-\alpha^{-1}},\\
&d_{00}^1(\zeta) = 1+\alpha\mathrm{Nu}-\alpha\mathrm{Nu}\,\mathrm{e}^{-(1-\zeta)\alpha^{-1}},\\
&d_{00}^2(\zeta) = \alpha\mathrm{Nu}+(1-\alpha\mathrm{Nu})\,\mathrm{e}^{-\zeta\alpha^{-1}},\\
&d_{00}^3(\zeta) = -(1+\alpha\mathrm{Nu})(1+\mathrm{Nu}\,\zeta)+\alpha\mathrm{Nu}\,(\mathrm{Nu}+2)\,\mathrm{e}^{-(1-\zeta)\alpha^{-1}}+\\
&\qquad+(1-\alpha\mathrm{Nu})\left[1+\mathrm{Nu}\,(1-\zeta)\right]\mathrm{e}^{-\alpha^{-1}}.
\end{aligned}\tag{A.2}$$

Similarly, the function $R_{0n}^3(\zeta)$, which is included in Equation (41), is a combination of the reradiation coefficients $R_{0n}^1(\zeta)$ and $R_{0n}^2(\zeta)$ of the n-mode axisymmetric thermal flow in the axial direction of the channel from its input and output cross-sections, respectively

$$\begin{aligned}
R_{0n}^3(\zeta) &= \mathrm{Nu}\left[R_{0n}^1(\zeta)\mathrm{e}^{-(s_{0n}^r-1)\zeta(2\alpha)^{-1}}+\right.\\
&\qquad\left.+\,R_{0n}^2(\zeta)\mathrm{e}^{-(s_{0n}^r+1)(1-\zeta)(2\alpha)^{-1}}\right],\\
R_{0n}^j(\zeta) &= \frac{d_{0n}^{jr}(\zeta)}{d_{0n}^{0r}}\qquad(j=1,2;\,n=1,2,3,\ldots)\,.
\end{aligned}\tag{A.3}$$

The temperature multipoles described by Equation (42) contain the functions $R_{mn}^{3r}(\zeta)$ and $R_{mn}^{3i}(\zeta)$, which have a complex physical nature of a combination of the reradiation coefficients of the asymmetric m-mode heat flux in the radial direction and n-mode in the axial direction (helix trajectory of heat rays) $R_{mn}^1(\zeta)$ and $R_{mn}^2(\zeta)$ $(m,n=1,2,3,\ldots)$:

$$\begin{aligned}
R_{mn}^{3r}(\zeta) &= R_{mn}^{1r}(\zeta)\left(\mathrm{Nu}I_{mn}^r-\mathrm{Nu}_m^i I_{mn}^i\right)-\\
&\quad-R_{mn}^{1i}(\zeta)\left(\mathrm{Nu}I_{mn}^i+\mathrm{Nu}_m^i I_{mn}^r\right)-\\
&\quad-R_{mn}^{2r}(\zeta)\left(\mathrm{Nu}J_{mn}^r+\mathrm{Nu}_m^i J_{mn}^i\right)+\\
&\quad+R_{mn}^{2i}(\zeta)\left(\mathrm{Nu}J_{mn}^i-\mathrm{Nu}_m^i J_{mn}^r\right),\\
R_{mn}^{3i}(\zeta) &= R_{mn}^{1r}(\zeta)\left(\mathrm{Nu}I_{mn}^i+\mathrm{Nu}_m^i I_{mn}^r\right)+\\
&\quad+R_{mn}^{1i}(\zeta)\left(\mathrm{Nu}I_{mn}^r-\mathrm{Nu}_m^i I_{mn}^i\right)-\\
&\quad-R_{mn}^{2r}(\zeta)\left(\mathrm{Nu}J_{mn}^r-\mathrm{Nu}_m^i J_{mn}^r\right)-\\
&\quad-R_{mn}^{2i}(\zeta)\left(\mathrm{Nu}J_{mn}^r+\mathrm{Nu}_m^i J_{mn}^i\right),
\end{aligned}\tag{A.4}$$

where

$$\begin{aligned}
R_{mn}^{1r}(\zeta) &= R_{mn}^1(\zeta)\,\mathrm{e}^{-(s_{mn}^r-1)\zeta(2\alpha)^{-1}}\times\\
&\quad\times\cos\left[\psi_{mn}^1(\zeta)-s_{mn}^i\zeta\,(2\alpha)^{-1}\right],\\
R_{mn}^{1i}(\zeta) &= R_{mn}^1(\zeta)\,\mathrm{e}^{-(s_{mn}^r-1)\zeta(2\alpha)^{-1}}\times\\
&\quad\times\sin\left[\psi_{mn}^1(\zeta)-s_{mn}^i\zeta\,(2\alpha)^{-1}\right],\\
R_{mn}^{2r}(\zeta) &= R_{mn}^2(\zeta)\,\mathrm{e}^{-(s_{mn}^r+1)(1-\zeta)(2\alpha)^{-1}}\times\\
&\quad\times\cos\left[\psi_{mn}^2(\zeta)-s_{mn}^i(1-\zeta)(2\alpha)^{-1}\right],\\
R_{mn}^{2i}(\zeta) &= R_{mn}^2(\zeta)\,\mathrm{e}^{-(s_{mn}^r+1)(1-\zeta)(2\alpha)^{-1}}\times\\
&\quad\times\sin\left[\psi_{mn}^2(\zeta)-s_{mn}^i(1-\zeta)(2\alpha)^{-1}\right].
\end{aligned}\tag{A.5}$$

$$\begin{aligned}
&I_{mn}^r=\cos\phi_{mn},\quad I_{mn}^i=\sin\phi_{mn},\\
&J_{mn}^r=\cos\left(\phi_{mn}-\frac{m\tan\phi_0}{\beta\varepsilon}\right),\\
&J_{mn}^i=\sin\left(\phi_{mn}-\frac{m\tan\phi_0}{\beta\varepsilon}\right),\\
&K_{mn}^r(\zeta)=\cos\left(\phi_{mn}-\frac{m\zeta\tan\phi_0}{\beta\varepsilon}\right),\\
&K_{mn}^i(\zeta)=\sin\left(\phi_{mn}-\frac{m\zeta\tan\phi_0}{\beta\varepsilon}\right),
\end{aligned}\tag{A.6}$$

Here also

$$\begin{aligned}
R_{mn}^j(\zeta) &= \sqrt{\frac{\left\{\left[d_{mn}^{jr}(\zeta)\right]^2+\left[d_{mn}^{ji}(\zeta)\right]^2\right\}}{\left[\left(d_{mn}^{0r}\right)^2+\left(d_{mn}^{0i}\right)^2\right]}},\\
\psi_{mn}^j(\zeta) &= \arctan\left[d_{mn}^{ji}(\zeta)/d_{mn}^{jr}(\zeta)\right]-\\
&\quad-\arctan\left(d_{mn}^{0i}/d_{mn}^{0r}\right)\quad(j=1,2)\,,
\end{aligned}\tag{A.7}$$

moreover

$$\begin{aligned} d_{mn}^{0r} &= 1-\left(s_{mn}^{r}+2\alpha\mathrm{Nu}\right)^{2}+s_{mn}^{i2}- \\ &\quad -\left\{\left[1-\left(s_{mn}^{r}-2\alpha\mathrm{Nu}\right)^{2}+s_{mn}^{i2}\right]\cos\left(s_{mn}^{i}\alpha^{-1}\right)- \right. \\ &\quad \left. -\,2s_{mn}^{i}\left(s_{mn}^{r}-2\alpha\mathrm{Nu}\right)\sin\left(s_{mn}^{i}\alpha^{-1}\right)\right\}\mathrm{e}^{-s_{mn}^{r}\alpha^{-1}}, \\ d_{mn}^{0i} &= -\,2s_{mn}^{i}\left(s_{mn}^{r}+2\alpha\mathrm{Nu}\right)+ \\ &\quad +\left\{\left[1-\left(s_{mn}^{r}-2\alpha\mathrm{Nu}\right)^{2}+s_{mn}^{i2}\right]\sin\left(s_{mn}^{i}\alpha^{-1}\right)+ \right. \\ &\quad \left. +\,2s_{mn}^{i}\left(s_{mn}^{r}-2\alpha\mathrm{Nu}\right)\cos\left(s_{mn}^{i}\alpha^{-1}\right)\right\}\mathrm{e}^{-s_{mn}^{r}\alpha^{-1}}, \end{aligned} \tag{A.8}$$

$$\begin{aligned} d_{mn}^{1r}(\zeta) &= 1+s_{mn}^{r}+2\alpha\mathrm{Nu}- \\ &\quad -\left\{\left(1-s_{mn}^{r}+2\alpha\mathrm{Nu}\right)\cos\left[s_{mn}^{i}\left(1-\zeta\right)\alpha^{-1}\right]- \right. \\ &\quad \left. -\,s_{mn}^{i}\sin\left[s_{mn}^{i}\left(1-\zeta\right)\alpha^{-1}\right]\right\}\mathrm{e}^{-s_{mn}^{r}(1-\zeta)\alpha^{-1}}, \\ d_{mn}^{1i}(\zeta) &= s_{mn}^{i}+\left\{\left(1-s_{mn}^{r}+2\alpha\mathrm{Nu}\right)\sin\left[s_{mn}^{i}\left(1-\zeta\right)\alpha^{-1}\right]+ \right. \\ &\quad \left. +\,s_{mn}^{i}\cos\left[s_{mn}^{i}\left(1-\zeta\right)\alpha^{-1}\right]\right\}\mathrm{e}^{-s_{mn}^{r}(1-\zeta)\alpha^{-1}}, \end{aligned} \tag{A.9}$$

$$\begin{aligned} d_{mn}^{2r}(\zeta) &= 1-s_{mn}^{r}-2\alpha\mathrm{Nu}- \\ &\quad -\left[\left(1+s_{mn}^{r}-2\alpha\mathrm{Nu}\right)\cos\left(s_{mn}^{i}\zeta\alpha^{-1}\right)+ \right. \\ &\quad \left. +\,s_{mn}^{i}\sin\left(s_{mn}^{i}\zeta\alpha^{-1}\right)\right]\mathrm{e}^{-s_{mn}^{r}\zeta\alpha^{-1}}, \\ d_{mn}^{2i}(\zeta) &= -\,s_{mn}^{i}+\left[\left(1+s_{mn}^{r}-2\alpha\mathrm{Nu}\right)\sin\left(s_{mn}^{i}\zeta\alpha^{-1}\right)- \right. \\ &\quad \left. -\,s_{mn}^{i}\cos\left(s_{mn}^{i}\zeta\alpha^{-1}\right)\right]\mathrm{e}^{-s_{mn}^{r}\zeta\alpha^{-1}}, \end{aligned} \tag{A.10}$$

where

$$\begin{aligned} s_{mn}^{r} &= \sqrt[4]{\left(1+\gamma^{2}\mu_{mn}^{2}\right)^{2}+\left(2\pi m\gamma^{2}\mathrm{Fo}_{0}^{-1}\right)^{2}}\times \\ &\quad \times\cos\left\{\tfrac{1}{2}\arctan\left[2\pi\mathrm{m}\gamma^{2}\mathrm{Fo}_{0}^{-1}\left(1+\gamma^{2}\mu_{\mathrm{mn}}^{2}\right)^{-1}\right]\right\}, \\ s_{mn}^{i} &= \sqrt[4]{\left(1+\gamma^{2}\mu_{mn}^{2}\right)^{2}+\left(2\pi m\gamma^{2}\mathrm{Fo}_{0}^{-1}\right)^{2}}\times \\ &\quad \times\sin\left\{\tfrac{1}{2}\arctan\left[2\pi\mathrm{m}\gamma^{2}\mathrm{Fo}_{0}^{-1}\left(1+\gamma^{2}\mu_{\mathrm{mn}}^{2}\right)^{-1}\right]\right\}. \end{aligned} \tag{A.11}$$

SYMBOLS

a	thermal diffusivity, $\mathrm{m}^2\cdot\mathrm{s}^{-1}$
$a_{mn}^{jl}(\cdot)$	complex function
$B_{mn}(\cdot)$	combination of cylindrical functions
c_j	complex coefficient
c_p	heat capacity of biomass, $\mathrm{J}\cdot\mathrm{kg}^{-1}\cdot\mathrm{K}^{-1}$
c_{mn}	coefficient
d	helix pitch, m
d_{00}^{0}	coefficient
$d_k^j(\cdot)$	intermediate function
$d_{mn}^{j}(\cdot)$	complex function
$d_{mn}^{jr}(\cdot)$	real part of complex function
$d_{mn}^{ji}(\cdot)$	imaginary part of complex function
d_{mn}^{0r}	real part of complex value
d_{mn}^{0i}	imaginary part of complex value
D_{mn}	modulus of complex value
$f(\cdot)$	intermediate function
Fo	Fourier number
Fo*	critical Fourier number
Fo_0	Fourier number corresponding to period τ_0
Fo_v	Fourier number corresponding to period τ_v
$g_{mn}(\cdot)$	partial function, s^{-1}
h	surface heat transfer coefficient, $\mathrm{W}/(\mathrm{m}^2\cdot\mathrm{K})$
I	current strength, A
I_{mn}^{r}	real part of complex function
I_{mn}^{i}	imaginary part of complex function
J_{mn}^{r}	real part of complex function
J_{mn}^{i}	imaginary part of complex function
$K_{mn}^{r}(\cdot)$	real part of complex function
$K_{mn}^{i}(\cdot)$	imaginary part of complex function
j	electric current density of the conductor, $\mathrm{A}\cdot\mathrm{m}^{-2}$
$J_m(\cdot)$	Bessel function of m-th order
L	length of reactor, m
$N_m(\cdot)$	Neumann function of m-th order
Nu	Nusselt number
Nu_m	complex Nusselt number
Nu_m^i	imaginary part of complex Nusselt number
p	Laplace transform parameter, s^{-1}
p_{mn}	poles, s^{-1}
$P_{mn}(\cdot)$	intermediate function
q_0	heat source intensity, $\mathrm{J}\cdot\mathrm{s}^{-1}\cdot\mathrm{m}^{-1}$
$q(\cdot)$	intensity function, $\mathrm{J}\cdot\mathrm{s}^{-1}\cdot\mathrm{m}$
r	radial variable, m
r_0	radius of helix cross-section, m
R_0	radius of helix, m
R_1	radius of channel, m
R_2	radius of shaft, m
$R_{mn}^{j}(\cdot)$	reradiation coefficient
$R_{mn}^{3r}(\cdot)$	real part of reradiation coefficient
$R_{mn}^{3i}(\cdot)$	imaginary part of reradiation coefficient
s_{mn}^{r}	real part of complex value
s_{mn}^{i}	imaginary part of complex value
$s_{mn}(\cdot)$	complex function
$s_{mn}^{\pm}(\cdot)$	complex function
S	cross-sectional area of the helix, m^2
T_0	initial temperature of biomass, K
T_{in}	temperature at channel entry, K
T_{out}	temperature at channel exit, K
T_c	constant temperature, K
$T(\cdot)$	temperature of biomass, K
$T_{mn}(\cdot)$	partial temperature, K
v	linear velocity of helix movement, m/s
v_0	velocity of biomass movement, m/s
v_m	complex velocity of biomass movement
v_0^*	critical velocity of biomass movement, m/s
w	specific strength of heat source, W/m^3
$W_{mn}^{j\mathrm{L}}(\cdot)$	complex function
$d_k^j(\cdot)$	intermediate function
x	intermediate variable
z	axial variable, m

Greek symbols

α	parameter
β	parameter
γ	parameter

$\delta(\cdot)$	Dirac function
δ_{mn}	Kronecker symbol
ε	dimensionless radius of helix
ε_0	dimensionless radius of shaft
ζ	dimensionless axial variable
θ	angular variable, rad
λ	coefficient of thermal conductivity, $\text{J}\cdot\text{s}^{-1}\cdot\text{m}^{-1}\cdot\text{K}^{-1}$
μ_{mn}	roots of transcendental equation
ξ	dimensionless radial variable
ρ	density of biomass, $\text{kg}\cdot\text{m}^{-3}$
ρ_0	electrical resistance of helix material, $\Omega\cdot\text{m}$
τ	time, s
τ_0	period of rotation of the helix, s
τ_v	period of rotation of the biomass particle, s
φ_0	angle of helix inclination, rad
φ_{mn}	partial phases, rad
Φ_{mn}	complex value
Φ^r_{mn}	real part of complex value
Φ^i_{mn}	imaginary part of complex value
$\psi^j_{mn}(\cdot)$	the phase function
ω	angular velocity of helix, Hz
ω_v	angular velocity of biomass particle rotation, Hz
$\Omega_{mn}(\cdot)$	intermediate function, K
$\Omega^0_{mn}(\cdot)$	intermediate function, K
$\vartheta(\cdot)$	dimensionless sensitivity function

Subscripts

0	initial
in	index
L	Laplace transform symbol
m	mode number
n	mode number
out	index
res	index

ACKNOWLEDGEMENTS

The authors express their gratitude to Prof. Zdzisław Pakowski for his interest in this topic.

REFERENCES

Biney M., Gusiatin M.Z., 2024. Biochar from co-pyrolyzed municipal sewage sludge (MSS): Part 1: Evaluating types of co-substrates and co-pyrolysis conditions. *Materials*, 17, 3603. DOI: 10.3390/ma17143603.

Brassard P., Godbout S., Raghavan V., 2017. Pyrolysis in auger reactors for biochar and bio-oil production: A review. *Biosystems Eng.*, 161, 80–92. DOI: 10.1016/j.biosystemseng.2017.06.020.

Bridgwater A.V., Bridge S.A., 1991. A review of biomass pyrolysis and pyrolysis technologies. In: Bridgwater A.V., Grassi G. (Eds.), *Biomass pyrolysis liquids upgrading and utilization*. Dordrecht: Springer, 11–92. DOI: 10.1007/978-94-011-3844-4_2.

Brown J.N., 2009. *Development of a lab-scale auger reactor for biomass fast pyrolysis and process optimization using response surface methodology*. MS Thesis, Iowa State University, Ames, Iowa.

Brown J.N., Brown R.C., 2012. Process optimization of an auger pyrolyzer with heat carrier using response surface methodology. *Bioresource Technol.*, 103, 405–414. DOI: 10.1016/j.biortech.2011.09.117.

Campuzano F., Brown R.C., Martínez J.D., 2019. Auger reactors for pyrolysis of biomass and wastes. *Renewable Sustainable Energy Rev.*, 102, 372–409. DOI: 10.1016/j.rser.2018.12.014.

Carslaw H.S., Jaeger J.C., 1959. *Conduction of heat in solids.* Clarendon Press, Oxford.

Chojnacki J., Kielar J., Najser J., Frantík J., Najser T., Mikeska M., Gaze B., Knutel B., 2024. Straw pyrolysis for use in electricity storage installations. *Heliyon*, 10, e30058. DOI: 10.1016/j.heliyon.2024.e30058.

Ding K., Xiong Q., Zhong Z., Zhong D., Zhang D., 2020. CFD simulation of combustible solid waste pyrolysis in a fluidized bed reactor. *Powder Technol.*, 362, 177–187. DOI: 10.1016/j.powtec.2019.12.011.

Dyke P.P.G., 2004. *An introduction to Laplace transforms and Fourier series*. Springer–Verlag, London.

Fryda L., Visser R., 2015. Biochar for soil improvement: evaluation of biochar from gasification and slow pyrolysis. *Agriculture*, 5, 1076–1115. DOI: 10.3390/agriculture5041076.

Ganesapillai M., Mehta R., Tiwari A., Sinha A., Bakshi H.S., Chellappa V., Drewnowski J., 2023. Waste to energy: A review of biochar production with emphasis on mathematical modelling and its applications. *Heliyon*, 9, e14873. DOI: 10.1016/j.heliyon.2023.e14873.

Garcia-Nunez J.A., Pelaez-Samaniego M.R., Garcia-Perez M.E., Fonts I., Abrego J., Westerhof R.J.M., Garcia-Perez M., 2017. Historical developments of pyrolysis reactors: A review. *Energy Fuels*, 13, 5751–5775. DOI: 10.1021/acs.energyfuels.7b00641.

Greco G., González B., Manyà J.J., 2019. Operating conditions affecting char yield and its potential stability during slow pyrolysis of biomass: a review. In: Manyà J.J. (Ed.), *Advanced carbon materials from biomass: an overview*. GreenCarbon ETN Book. Green Carbon Project and Consortium, 9–19. DOI: 10.5281/zenodo.3233733.

Hasan M.M., Rasul M.G., Jahirul M.I., Khan M.M.K., 2024. Fast pyrolysis of municipal green waste in an auger reactor: Effects of residence time and particle size on the yield and characteristics of produced oil. *Energies*, 17, 2914. DOI: 10.3390/en17122914.

Igliński B., Kujawski W., Kiełkowska U., 2023. Pyrolysis of waste biomass: technical and process achievements, and future development. – A review. *Energies*, 16, 1829. DOI: 10.3390/en16041829.

Jalalifar S., Abbassi R., Garaniya V., Salehi F., Papari S., Hawboldt K., Strezov V., 2020. CFD analysis of fast pyrolysis process in a pilot-scale auger reactor. *Fuel*, 273, 117782. DOI: 10.1016/j.fuel.2020.117782.

Korn G.A., Korn T.U., 2000. *Mathematical handbook for scientists and engineers: definitions, theorems and formulas for references and review.* 2nd revised edition, Dover Publications, New York.

Ledakowicz S., Piddubniak O., 2021. Analysis of non-stationary temperature field generated by a shaftless screw conveyor heated by Joule–Lenz effect. *Chem. Process. Eng.*, 42, 119–137. DOI: 10.24425/cpe.2021.138920.

Ledakowicz S., Piddubniak O., 2022. The non-stationary heat transport inside a shafted screw conveyor filled with homogeneous biomass heated electrically. *Energies*, 15, 6164. DOI: 10.3390/en15176164.

Ledakowicz S., Piddubniak O., 2023. Temperature distribution in a finite-length cylindrical channel filled with biomass transported by electrically heated auger. *Energies*, 16, 6260. DOI: 10.3390/en16176260.

Ledakowicz S., Stolarek P., Malinowski A., Lepez O., 2019. Thermochemical treatment of sewage sludge by integration of drying and pyrolysis/autogasification. *Renewable Sustainable Energy Rev.*, 104, 319–327. DOI: 10.1016/j.rser.2019.01.018.

Lepez O., Sajet P., 2009. *Device for the thermal processing of divided solids* EP 2218300 A2 20100818 (FR). Patent EP 2218300, WO2009095564A2, 6 August 2009.

Lewandowski W.M., Januszewicz K., Kosakowski W., 2019. Efficiency and proportions of waste tyre pyrolysis products depending on the reactor type – A review. *J. Anal. Appl. Pyrolysis*, 140, 25–53. DOI: 10.1016/j.jaap.2019.03.018.

Luikov A. V., 1968. *Analytical heat diffusion theory.* Academic Press Inc. Ltd, London.

Luz F C, Cordiner S., Manni A., Mulone V., Rocco V., 2018. Biomass fast pyrolysis in a shaftless screw reactor: A 1-D numerical. *Energy,* 157, 792–805. DOI: 10.1016/j.energy.2018.05.166.

Luz F.C., Cordiner S., Manni A., Mulone V., Rocco V., 2017. Pyrolysis in screw reactors: a 1-D numerical tool. *Energy Procedia*, 126, 683–689. DOI: 10.1016/j.egypro.2017.08.297.

Makkawi Y., Pour F.H., Elsayed Y., Khan M., Moussa O., Masek O., Badrelzaman M., El Tahir W., 2022. Recycling of post-consumption food waste through pyrolysis: Feedstock characteristics, products analysis, reactor performance, and assessment of worldwide implementation potentials. *Energy Convers. Manage.*, 272, 116348. DOI: 10.1016/j.enconman.2022.116348.

Maximino R., 2013. *Pyrolysis of biomass residues in a screw reactor.* MS. Thesis, Lisbon, Portugal. Available at: https://fenix.tecnico.ulisboa.pt/downloadFile/395146017998/artigo_ricardo.pdf

Morgano M.T., 2019. *Screw pyrolysis of biogenic feedstock with integrated hot gas filtration.* Dr.-Ing. Thesis, Institute of Combustion and Power Plant Technology (IFK), University of Stuttgart. Available at: https://elib.uni-stuttgart.de/bitstream/11682/10434/1/Dissertation-Tomasi-Morgano.pdf.

Moser K., Wopienka E., Pfeifer C., Schwarz M., Sedlmayer I., Haslinger W., 2023. Screw reactors and rotary kilns in biochar production – A comparative review. *J. Anal. Appl. Pyrolysis*, 174, 106112. DOI: 10.1016/j.jaap.2023.106112.

Nachenius R.W, van de Wardt T.A., Ronsse F., Prins W., 2015a. Residence time distributions of coarse biomass particles in a screw conveyor reactor. *Fuel Process. Technol.*, 130, 87–95. DOI: 10.1016/j.fuproc.2014.09.039.

Nachenius R.W, van de Wardt T.A., Ronsse F., Prins W., 2015b. Torrefaction of pine in a bench-scale screw conveyor reactor. *Biomass Bioenergy*, 79, 96–104. DOI: 10.1016/j.biombioe.2015.03.027.

Obrycki T.Z., Sztaba B., Jaszek P.W., Zmuda W.A., 2017. *A method and a reactor for thermal pyrolysis of rubber materials*, 20.04.2017, PCT/EP2016/074632. Patent WO/2017/064211.

Ore O.T., Adebiyi F.M., 2021. A review on current trends and prospects in the pyrolysis of heavy oils. *J. Petrol. Explor. Prod. Technol.*, 11, 1521–1530. DOI: 10.1007/s13202-021-01099-0.

Partridge A.H, Casini I., McKahn D.A., Carter D., Chamberlin C., Jacobson A., Palmer K., Rana Y., Severy M., 2023. *Influence of temperature, feedstock and moisture content in a continuous feed screw torrefier.* Engineering: Faculty Publications, Smith College, Northampton, MA. Available at: https://scholarworks.smith.edu/egr_facpubs/152/.

Perera S.M.H.D., Wickramasinghe C., Samarasiri B.K.T., Narayana M., 2021. Modeling of thermochemical conversion of waste biomass – a comprehensive review. *Biofuel Res. J.,* 32, 1481–1528. DOI: 10.18331/brj2021.8.4.3.

Pflanz E., 1948. Über eine Verallgemeinerung des Verfahrens der Kombination von Newton'scher Methode und Regula falsi zur Auflosung einer Gleichung $f(x)=0$. *Z. Angew. Math. Mech.*, 28, 114–122.

Piddubniak O., Ledakowicz S., 2022. Modeling of heat transfer from an electrically heated rotating helix in a circular cylindrical channel filled with a biomass moving at a constant velocity. *Therm. Sci. Eng. Prog.*, 30, 101265. DOI: 10.1016/j.tsep.2022.101265.

Piersa P., Unyay H., Szufa S., Lewandowska W., Modrzewski R., Ślęzak R., Ledakowicz S., 2022. An extensive review and comparison of modern biomass torrefaction reactors vs. biomass pyrolysis – Part 1. *Energies*, 15, 2227. DOI: 10.3390/en15062227.

Pilát P., Patsch M., 2022. Utilization of the energy potential of waste from the automotive industry. *40th Annual Conference – Meeting of the Departments of Fluid Mechanics and Thermomechanics in the connection with XXIII. International Scientific Conference – The Application of Experimental and Numerical Methods in Fluid Mechanics and Energy*. MATEC Web of Conferences 369, 03004. DOI: 10.1051/matecconf/202236903004.

Proãno A.G.C., 2024. *Combined multi-scale modelling and experimentation for lignin-rich biomass pyrolysis.* PhD Thesis, University College London, Department of Chemical Engineering. Available at: https://discovery.ucl.ac.uk/id/eprint/10188014.

Raza M., Inayat A., Ahmed A., Jamil F., Ghenai C., Naqvi S.R., Shanableh A., Ayoub M., Waris A., Park Y.-K., 2021. Progress of the pyrolyzer reactors and advanced technologies for biomass pyrolysis processing. *Sustainability*, 13, 11061. DOI: 10.3390/su131911061.

Rego F.A.H., 2021. *Continuous slow pyrolysis of wheat straw in a screw reactor and use of the char for water decontamination.* PhD Thesis, Aston University. Available at: https://publications.aston.ac.uk/id/eprint/43440/1/REGO_FILIPE_ANTONIO_HENRIQUES_2021.pdf.

Sanchís A., Veses A., Martínez J.D., López J.M., García T., Murillo R., 2022. The role of temperature profile during the pyrolysis of end-of-life-tyres in an industrially relevant conditions auger plant. *J. Environ. Manag.*, 317, 115323. DOI: 10.1016/j.jenvman.2022.115323.

Shutterstock, 2024. https://www.shutterstock.com/image-vector/set-augers-archimedes-screw-bit-used-1716194236. Accessed 22 November 2024.

Shi X., Ronsse F., Nachenius R.W., Pieters J.G., 2019. 3D Eulerian–Eulerian modeling of a screw reactor for biomass thermochemical conversion. Part 2: Slow pyrolysis for char production. *Renewable Energy*, 143, 1477–1487. DOI: 10.1016/j.renene.2019.05.088.

Spirajoule®NA, 2025. Spirajoule Brochure. Revolutionary concept and design in heat exchanger technology. Available at: https://www.scribd.com/document/620925649/Spirajoule-Brochure.

Teo S.H., Gan H.L., Alias A., Gan L.M., 2018. Internally heated screw pyrolysis reactor (IHSPR) heat transfer performance study. *IOP Conf. Ser.: Mater. Sci. Eng.*, 342, 012096. DOI: 10.1088/1757-899X/342/1/012096.

Ubiera Ruiz L.A., 2021. *Development of a microwave pyrolysis process applied to flax shives and sargassum: product characterization and wave-matter interaction.* PhD Thesis, Chemical and Process Engineering. Normandie Université. NNT: 2021NORMIR34. Available at: https://theses.hal.science/tel-03667954v1/file/UBIERARUIZ.pdf.

Verclyte A., 2013. *Mass and heat transfer modelling in screw reactors.* MSc. Theses, Ghent University. https://libstore.ugent.be/fulltxt/RUG01/002/063/502/RUG01-002063502_2013_0001_AC.pdf.

Vikram S., Rosha P., Kumar S., 2021. Recent modeling approaches to biomass pyrolysis: A review. *Energy Fuels*, 35, 7406–7433. DOI: 10.1021/acs.energyfuels.1c00251.

Wang M., Wu Y., Jiang E., Chen X., 2015. Biomass continuous pyrolysis characteristics on shaftless screw conveying reactor. *Trans. Chin. Soc. Agric. Eng.,* 31 (15), 216–222. DOI: 10.11975/j.issn.1002-6819.2015.15.030.

Winchell L.J., Ross J.J., Brose D.A., Pluth T.B , Fonoll X., Norton J.W. Jr, Bell K.Y., 2022. Pyrolysis and gasification at water resource recovery facilities: Status of the industry, *Water Environ. Res.*, 94, e10701. DOI: 10.1002/wer.10701.

Wu P., Ata-Ul-Karim S.T., Singh B.P., Wang H., Wu T., Liu C., Fang G., Zhou D., Wang Y., ChenW., 2019. A scientometric review of biochar research in the past 20 years (1998–2018). *Biochar*, 1, 23–43. DOI: 10.1007/s42773-019-00002-9.

Zerin N.H., Rasul M.G., Jahirul M.I., Sayem A.S.M., 2023. End-of-life tyre conversion to energy: A review on pyrolysis and activated carbon production processes and their challenges. *Sci. Total Environ.,* 905, 166981. DOI: 10.1016/j.scitotenv.2023.166981.

Zhao F., Li Y., Liu Z., 2024. Numerical study on pyrolysis characteristics of oil-based drilling cuttings in a two-layer screw-driving spiral heat exchanger. *Clean Energy Sustainability*, 2, 10008. DOI: 10.35534/ces.2024.10008.

Zhao F., Li Y., Liu Z., Tang Y., 2020. Flow and heat transfer characteristics of oil-based drilling cuttings in a screw-driving spiral heat exchanger. *Appl. Thermal Eng.*, 181, 115881. DOI: 10.1016/j.applthermaleng.2020.115881.